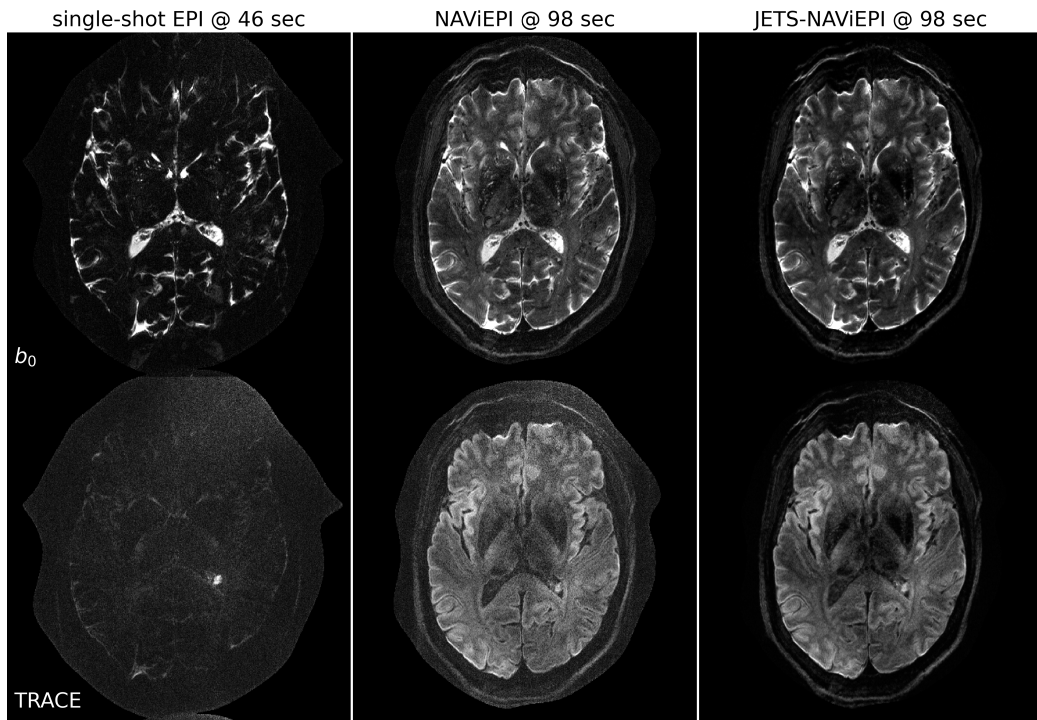


Graphical Abstract

Accelerated Diffusion Weighted Magnetic Resonance Imaging at 7 T: Joint Reconstruction for Shift-Encoded Navigator-based Interleaved Echo Planar Imaging (JETS-NAViEPI)

Zhengguo Tan, Patrick Alexander Liebig, Robin Martin Heidemann, Frederik Bernd Laun, Florian Knoll

3-scan trace acquisition with voxel size 0.5 X 0.5 X 2.0 mm³



Highlights

Accelerated Diffusion Weighted Magnetic Resonance Imaging at 7 T: Joint Reconstruction for Shift-Encoded Navigator-based Interleaved Echo Planar Imaging (JETS-NAViEPI)

Zhengguo Tan, Patrick Alexander Liebig, Robin Martin Heidemann, Frederik Bernd Laun, Florian Knoll

- Navigator-based interleaved EPI acquisition with minimal distortion mismatch between echoes
- Novel accelerated diffusion acquisition with shifted phase encoding among diffusion directions for complementary k - q -space sampling at 7 T
- Generalized joint k - q -slice diffusion-weighted image reconstruction with overlapping locally low-rank regularization
- Efficient simultaneous multi-slice (SMS) image reconstruction
- 3-scan trace acquisition with the voxel size $0.5 \times 0.5 \times 2.0 \text{ mm}^3$ and 60 slices at 1.5 min

Accelerated Diffusion Weighted Magnetic Resonance Imaging at 7 T: Joint Reconstruction for Shift-Encoded Navigator-based Interleaved Echo Planar Imaging (JETS-NAViEPI)

Zhengguo Tan^a, Patrick Alexander Liebig^b, Robin Martin Heidemann^b,
Frederik Bernd Laun^c, Florian Knoll^a

^a*Department Artificial Intelligence in Biomedical Engineering (AIBE),
Friedrich-Alexander University of Erlangen-Nuremberg, Erlangen, Germany*

^b*Siemens Healthcare GmbH, Erlangen, Germany*

^c*Institute of Radiology, University Hospital Erlangen, Friedrich-Alexander University of Erlangen-Nuremberg, Erlangen, Germany*

Abstract

The pursuit of high spatial-angular-temporal resolution for in vivo diffusion-weighted magnetic resonance imaging (DW-MRI) at ultra-high field strength (7 T and above) is important in understanding brain microstructure and function. Such pursuit, however, faces several technical challenges. First, increased off-resonance and shorter T_2 relaxation require faster echo train readouts. Second, existing high-resolution DW-MRI techniques usually employ in-plane fully-sampled multi-shot EPI, which not only prolongs the scan time but also induces a high specific absorption rate (SAR) at 7 T. To address these challenges, we develop in this work navigator-based interleaved EPI (NAViEPI) which enforces the same effective echo spacing (ESP) between the imaging and the navigator echo. First, NAViEPI renders no distortion mismatch between the two echoes, and thus simplifies shot-to-shot phase variation correction. Second, NAViEPI allows for a large number of shots

(e.g. > 4) with undersampled iEPI acquisition, thereby rendering clinically-feasible high-resolution sub-millimeter protocols. To retain signal-to-noise ratio (SNR) and to reduce undersampling artifacts, we developed a k_y -shift encoding among diffusion encodings to explore complementary k - q -space sampling. Moreover, we developed a novel joint reconstruction with overlapping locally low-rank regularization generalized to the multi-band multi-shot acquisition at 7 T (dubbed JETS-NAViEPI). Our method was demonstrated with experimental results covering 1 mm isotropic resolution multi b -value DWI and sub-millimeter in-plane resolution fast TRACE acquisition.

Keywords: Diffusion-weighted magnetic resonance imaging, Echo planar imaging, Navigator, Ultra-high field, Joint reconstruction, Low rank, Simultaneous multi slice

¹ **1. Introduction**

² Diffusion-weighted magnetic resonance imaging (DW-MRI) ([Le Bihan et al., 1986; Merboldt et al., 1985](#)) is a non-invasive modality that is sensi-
³ tive to the intravoxel Brownian motion of water molecules. DW-MRI forms
⁴ the basis for diffusion tensor imaging (DTI) ([Basser et al., 1994; Mori et al., 1999](#)) and high angular resolution diffusion imaging (HARDI) ([Tuch et al., 2002](#)), and has been widely used in acute brain ischemia diagnosis, in tumor
⁵ detection and staging, and in neuroscience ([Jones, 2010](#)).

⁶ For DW-MRI acquisition, the commonly used pulse sequence is single-
⁷ shot echo-planar imaging (SS-EPI) ([Mansfield, 1977](#)). SS-EPI is capable of
⁸ rapidly acquiring one DW image per radio-frequency excitation at the order
⁹ of 100 ms, and is thus motion robust. However, conventional SS-EPI, even
¹⁰ with three-fold accelerated acquisition ([Bammer et al., 2001](#)) using parallel
¹¹ imaging ([Roemer et al., 1990; Ra and Rim, 1993; Pruessmann et al., 1999](#);
¹² [Griswold et al., 2002](#)), still suffers from low spatial resolution and geometric
¹³ distortions.

¹⁴ In the quest for high spatial-angular-temporal-resolution and minimal-
¹⁵ geometry-distortion DW-MRI, tremendous efforts have been made. Tech-
¹⁶ niques [for](#) the correction of image distortions induced by off-resonances and R249.Minor.5
¹⁷ eddy currents have been developed ([Andersson et al., 2003](#)). Furthermore,
¹⁸ gSlider ([Setsompop et al., 2018](#)) with blipped-CAIPI ([Setsompop et al., 2012](#))
¹⁹ for simultaneous multi-slice (SMS) ([Maudsley, 1980; Breuer et al., 2005](#))
²⁰ was proposed to achieve high-resolution DW-MRI. Advanced pulse sequences
²¹ based on multi-shot EPI have also been developed, including but not limited
²² to interleaved EPI (iEPI) ([Butts et al., 1993](#)), PROPELLER ([Pipe et al., 2004](#)),

26 2002), and readout-segmented EPI (rsEPI) (Porter and Heidemann, 2009;
27 Heidemann et al., 2010).

28 Based on four-shot iEPI, multiplexed sensitivity encoding (MUSE) image
29 reconstruction achieved DW-MRI with a sub-millimeter in-plane resolution
30 and maximal b -value 800 s/mm^2 at 3 T (Chen et al., 2013). The four-shot
31 iEPI employed in MUSE acquired an in-plane fully-sampled k -space, except
32 partial Fourier. Every shot (segment), corresponding to four-fold under-
33 sampling, was then reconstructed via parallel imaging to obtain shot-to-shot
34 phase variation. This indicates that increasing the number of shots in MUSE
35 will result in higher undersampling per shot, and consequently, degrade shot
36 phase estimation (Wu and Miller, 2017).

37 Alternatively, navigator-based iEPI acquisition has been proposed (Jeong
38 et al., 2013; Dai et al., 2017, 2018). These proposals allow for a larger num-
39 ber of shots, and hence higher spatial resolution. However, due to the use of
40 different ESP between the imaging echo and the navigator echo, these pro-
41 posals suffered from geometric distortion mismatch between the two echoes
42 and thus required specific compensation methods. In contrast, rsEPI (Porter
43 and Heidemann, 2009; Heidemann et al., 2010) used the same readout seg-
44 ment for both echoes, and thus required no distortion correction of navigator
45 echoes.

46 Beyond the MUSE-type parallel imaging reconstruction, compressed sens-
47 ing (Lustig et al., 2007; Block et al., 2007) has been explored. For instance,
48 multi-shot reconstruction techniques based on structured low-rank matrix
49 completion (MUSSELS) (Mani et al., 2017; Bilgic et al., 2019) achieved 5-
50 shot DW-MRI with 9-fold undersampling per shot. Recently, JULEP (Dai

51 et al., 2023) incorporated explicit phase mapping into MUSSELS. These re-
52 construction techniques, i.e., MUSE, MUSSELS and JULEP, targeted the
53 reconstruction of one DW image from interleaved EPI acquisition, and did
54 not explore joint- k - q -space undersampling or reconstruction.

55 Joint- k - q -space undersampling can be achieved via proper regularization
56 along the diffusion encoding direction. Relevant examples are diffusion un-
57 dersampling with Gaussian process estimated reconstruction (DAGER) (Wu
58 et al., 2019) and magnitude-based spatial-angular locally low-rank regular-
59 ization (SPA-LLR) (Hu et al., 2020). However, DAGER addressed the re-
60 construction problem of single-shot EPI acquisition and SPA-LLR focused
61 on the reconstruction of single-band and fully-sampled iEPI acquisition. R248.Major.2

62 In this work, we propose a Joint k - q -slice rEconsTruction framework
63 for Shift-encoded NAVigator-based interleaved EPI at 7 T (dubbed JETS-
64 NAViEPI). Our pulse sequence, NAViEPI, differs from most existing tech-
65 niques. First, NAViEPI builds upon interleaved EPI, thereby allowing for
66 fast and efficient k -space coverage. Second, inspired by rsEPI, NAViEPI en-
67 sures the same effective ESP between the imaging and the navigator echo,
68 thereby minimizing geometric distortion and allowing for the use of a larger
69 number of shots. NAViEPI essentially integrates the advantages of both iEPI
70 and rsEPI. Third, NAViEPI utilizes undersampled multi-shot iEPI, thereby
71 alleviating the SAR problem at 7 T. Fourth, NAViEPI shifts the k -space in-
72 plane sampling pattern along the phase encoding (k_y) direction. This shifting
73 creates complementary k - q -space sampling, which leads to the possibility of
74 our joint k - q -slice reconstruction. Specifically, we employ spatial-diffusion
75 overlapping LLR regularization to jointly reconstruct all diffusion encodings

⁷⁶ and multi-band slices. In vivo experiments at 7 T and comparisons with other
⁷⁷ techniques demonstrate the efficiency of our proposed method in achieving
⁷⁸ high spatial resolution DW-MRI at ultra-high field.

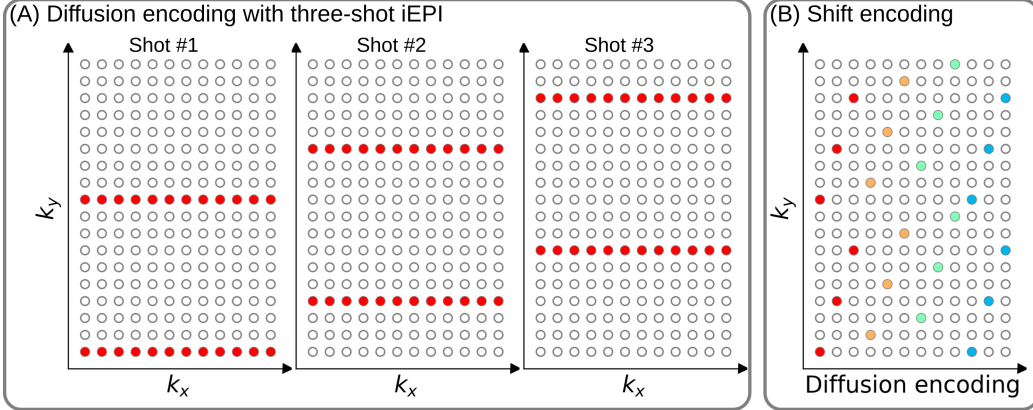


Figure 1: (A) An example DW-MRI acquisition with three-shot interleaved EPI acquisition. (B) The proposed k_y shifted diffusion encoding scheme. This example employs three shots per DW image. Therefore, every three columns have the same color.

79 2. Materials and methods

80 2.1. Multi-band shift-encoded iEPI acquisition

81 Fig. 1 (A) displays the diffusion-weighted image acquisition based on
 82 three-shot interleaved EPI with three-fold in-plane undersampling. Conven-
 83 tionally, such a sampling pattern is repeated for all diffusion directions. In
 84 contrast, we propose the k_y -shifted diffusion encoding, as shown in Fig. 1 (B).
 85 The interleaved EPI sampling pattern is shifted by one k_y line per diffusion
 86 direction, with the cycling period being the in-plane undersampling factor.

87 It is worth noting that, as shown in Fig. 1 (A), the undersampling factor
 88 of one segment is $R_{\text{in-plane}} \times N_{\text{shot}}$ (ignore multi-band undersampling here),
 89 yielding nine-fold in-plane undersampling in this example. In other words,
 90 the undersampling factor per segment linearly scales up with the number
 91 of shots. Consequently, conventional self-gating reconstruction techniques,
 92 e.g. MUSE, suffer from degraded shot-to-shot phase estimation, which in

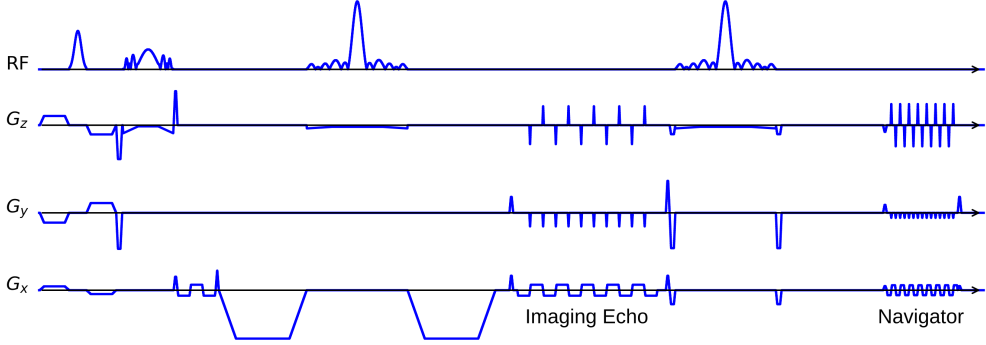


Figure 2: The NAViEPI sequence diagram. SMS is utilized for the acquisition of both imaging and navigator echoes. While the acceleration factor per navigator is the same as listed in Table 1, the acceleration factor per imaging echo is in addition linearly scaled by the number of shots.

93 turn limits the number of shots and spatial resolution.

94 *2.2. NAViEPI: Navigator-based iEPI with consistent effective ESP between
95 the imaging and the navigator echo - where iEPI meets rsEPI*

96 Instead of the self-gated MUSE with in-plane fully-sampled iEPI and
97 a limited number of shots, We propose NAVigator-based interleaved EPI
98 (NAViEPI), as illustrated in Fig. 2. Inspired by rsEPI (Porter and Hei-
99 demann, 2009), NAViEPI enforces a consistent effective ESP between the
100 imaging and the navigator echo, thereby minimizing distortion mismatch
101 between the two echoes.

102 Since one imaging echo presents one segment in multi-shot EPI acquisi-
103 tion, its effective ESP is defined as

$$\text{ESP}_{\text{eff}} = \frac{\text{ESP}}{R_{\text{in-plane}} \times N_{\text{shot}}} \quad (1)$$

104 Here, a larger number of shots (segments) increases the undersampling factor
105 per segment (see Fig. 1), but decreases the effective ESP. Since the navigator

106 echo is acquired for each segment, its in-plane undersampling factor equals
107 $R_{\text{in-plane}}$. Therefore, the effective ESP of the navigator echo must match that
108 of the imaging echo, as given in Eq. (1). With a matching effective ESP, the
109 base resolution of the navigator echo can then be determined.

110 *2.3. In vivo acquisition protocols*

111 We implemented multiple in-vivo acquisition protocols at a clinical 7 T
112 MR system (MAGNETOM Terra, Siemens Healthineers, Erlangen, Ger-
113 many) equipped with a 32-channel head coil (Nova Medical, Wilmington,
114 MA, USA) and the XR-gradient system (maximum gradient strength 80 mT/m
115 with a peak slew rate of 200 T/m/s). To calibrate coil sensitivity maps, refer-
116 ence scans employed a gradient-echo (GRE) sequence. Spectral fat saturation
117 and mono-polar diffusion-encoding gradients were used. The phase-encoding
118 direction was selected as anterior-to-posterior.

Table 1: NAViEPI acquisition protocols

Protocol	1.0 mm isotropic		sub-millimeter	
	#1	#2	#3	#4
Diffusion mode	MDDW ⁽¹⁾		3-scan trace	
Diffusion scheme	monopolar			
Diffusion direction	20	114	3	
<i>b</i> -value (s/mm ²)	1000	3-shell ⁽²⁾	1000	
<i>b</i> ₀	0	12	1	
FOV (mm ²)	200	214	220	
In-plane resolution (mm ²)	1.0		0.5	
Slice thickness (mm)	1.0		2.0	
Slices	141	114	60	
Navigator	No	No	Yes	No
Shots	4	2	5	1
TR (ms)	7700	5200	4400	8000
TEs (ms)	67	66	58/95.1	143
ESP (ms)	1.02	0.81	1.52	1.48
Bandwidth (Hz/Pixel)	1086	1460	758	
Partial Fourier			6/8	
Acceleration ⁽³⁾	1 × 3	3 × 3	3 × 2	
TA (min) ⁽⁴⁾	10 : 42	22 : 25	1 : 38	0 : 46

⁽¹⁾ MDDW: Multi-direction diffusion weighting;

⁽²⁾ 3-shell: 20, 30, and 64 directions with *b*-values of 1000, 2000, and 3000 s/mm², respectively;

⁽³⁾ Acceleration: Both in-plane and slice undersampling can be employed, denoted as (*R*_{in-plane} × *R*_{slice});

⁽⁴⁾ TA: Total acquisition time.

120 This study was approved by the local ethics committee. Three volunteers
121 with informed consent obtained before scanning participated in this study.
122 Detailed acquisition protocols are listed in Table 1.

123 *2.3.1. 20-diffusion-direction acquisition at 1 mm isotropic resolution*

124 As listed in Table 1, Protocol #1 with four-shot iEPI and without in- R248.Major.1a
125 plane undersampling was implemented. This protocol represents the acquisi-
126 tion scheme employed in many existing multi-shot reconstruction techniques,
127 (e.g., MUSE, SPA-LLR, and JULEP). The acquired data from this protocol
128 served as ground truth. Different reconstruction methods, specifically JETS,
129 MUSE, and JULEP were compared. We compared with JULEP instead of R249.Minor.6
130 MUSSELS, because JULEP uses not only structured low-rank constraints R248.Major.3a
131 but also explicit phase mapping.

132 We then retrospectively reduced the four-shot data to only one shot per R248.Major.1b
133 diffusion encoding without and with the proposed k_y shifting to simulate
134 four-fold in-plane undersampling. JETS reconstruction was performed on R248.Major.1b
135 the fully-sampled data and the retrospectively undersampled data to validate
136 the proposed k_y -shifted acquisition. R248.Major.1c

137 *2.3.2. Three-shell acquisition at 1 mm isotropic resolution*

138 Protocol #2 in Table 1 was implemented for multi-shell diffusion tensor R248.Major.3c
139 imaging (DTI) (Basser et al., 1994). We acquired a total of 114 diffusion
140 directions, whereas b_0 measurements were interspersed every ten diffusion
141 directions. This protocol was used to demonstrate the capability of of JETS
142 in achieving high spatial-angular-temporal resolution.

₁₄₃ 2.3.3. 3-scan trace acquisition at $0.5 \times 0.5 \times 2.0 \text{ mm}^3$ voxel size

₁₄₄ As listed in Table 1, Protocol #3 was implemented based on NAViEPI
₁₄₅ with five shots per diffusion encoding. This protocol was compared against
₁₄₆ single-shot EPI (Protocol #4) with the same spatial resolution and acceler-
₁₄₇ ation, such as to demonstrate the sampling efficiency of NAViEPI.

₁₄₈ 2.4. Forward modeling

₁₄₉ Our proposed acquisition method yields multi-dimensional multi-band
₁₅₀ k -space data $\mathbf{y}_{c,q,s}$, where c, q, s denotes the index of the coil sensitivity
₁₅₁ map, the diffusion encoding, and the shot, respectively. Acquisition modeling
₁₅₂ needs to consider several aspects.

₁₅₃ First, the acquired k -space data \mathbf{y} is mapped from individual shot images
₁₅₄ $\mathbf{x}_{q,s,z}$ via the forward model,

$$\begin{aligned}\mathbf{y}_{c,q,s} &= \mathbf{P}_{q,s} \boldsymbol{\Sigma} \boldsymbol{\Theta}_z \mathbf{F} \mathbf{S}_c \mathbf{x}_{q,s,z} \\ \mathbf{y} &:= \mathbf{E}_1 \mathbf{x}\end{aligned}\tag{2}$$

₁₅₅ Here, the encoding matrix \mathbf{E}_1 comprises a chain of linear operators. Every
₁₅₆ shot image \mathbf{x} is point-wise multiplied by a set of coil sensitivity maps (\mathbf{S}) and
₁₅₇ Fourier transformed (\mathbf{F}). The output is then point-wise multiplied by the
₁₅₈ multi-slice phase map ($\boldsymbol{\Theta}$) with z the slice index in simultaneously excited
₁₅₉ slices. This operator shifts individual slice along the phase-encoding direction
₁₆₀ via varying phase modulation (Breuer et al., 2005). The SMS k -space data
₁₆₁ is then summed (collapsed, $\boldsymbol{\Sigma}$) along the slice dimension and masked (point-
₁₆₂ wise multiplied, \mathbf{P}) by the sampling pattern of each diffusion encoding and
₁₆₃ shot.

164 Second, for diffusion MRI based on multi-shot EPI, multiple shots ac-
 165 quired for a given diffusion encoding need to be combined as one DW image
 166 ($\tilde{\mathbf{x}}$). One possibility is to perform magnitude average (Chen et al., 2013)
 167 or root-sum-squares (RSS) (Mani et al., 2017) of shot images. This method R249.Minor.7
 168 is robust to in-plane motion, but sub-optimal concerning SNR (Guhaniyogi
 169 et al., 2016). Alternatively, shot combination can be done via shot-to-shot
 170 phase variation correction (Liu et al., 2005; Chen et al., 2013). This can be
 171 incorporated into our formulation as point-wise multiplication between the R249.Minor.8
 172 shot-to-shot phase variation (Φ) and the DW image ($\tilde{\mathbf{x}}$),

$$\mathbf{x}_{q,s,z} = \Phi_{q,s,z} \tilde{\mathbf{x}}_{q,z} \quad (3)$$

173 Note that $\tilde{\mathbf{x}}$ can be obtained by applying the adjoint of Φ to \mathbf{x} . In MUSE,
 174 Φ is obtained by parallel imaging reconstruction of all shots with subsequent
 175 phase smoothing of every shot image. Based on this phase correction, the
 176 complete forward model follows

$$\mathbf{y} := \mathbf{E}_2 \tilde{\mathbf{x}} = \mathbf{E}_1 \Phi \tilde{\mathbf{x}} \quad (4)$$

177 where the encoding matrix \mathbf{E}_2 comprises the chain of the shot-to-shot phase
 178 variation Φ and the encoding matrix \mathbf{E}_1 . We implemented these two encoding
 179 operators in SigPy (Ong and Lustig, 2019).

180 *2.5. Joint k - q -slice reconstruction*

181 Based on the generalized forward models in Eqs. (2) and (4), our proposed
 182 joint k - q -slice reconstruction can be formulated as a three-step approach.

183 **I. Navigator echo reconstruction.** The acquisition of navigator echoes
 184 follows the forward model in Eq. (2), so the reconstruction of navigator

185 echoes can be formulated as:

$$\operatorname{argmin}_{\mathbf{x}} \|\mathbf{y} - \mathbf{E}_1 \mathbf{x}\|_2^2 + \lambda \mathbf{R}(\mathbf{x}) \quad (5)$$

186 where $\mathbf{R}(\mathbf{x})$ denotes the regularization functional with the regularization
187 strength λ . In this work, ℓ^2 regularization was used, i.e., $\mathbf{R}(\mathbf{x}) =$
188 $\|\mathbf{x}\|_2^2$. In the case of self-navigating (i.e., no navigator acquired) as
189 Protocol #2, the central k -space region (i.e., 1/4 of the full image matrix)
190 of each segment is used as \mathbf{y} in Eq. (5).

191 **II. Iterative phase smoothing.** Shot-to-shot phase variation was ex-
192 tracted from the reconstructed navigator echo phases. Assuming that
193 phase images are spatially smooth (Chen et al., 2013; Dai et al., 2023),
194 we employed the iterative approach to smooth phase,

$$\mathbf{x}^{(k+1)} = \mathbf{F}^{-1} \mathcal{H} \mathbf{F} \mathbf{x}^{(k)} \quad (6)$$

195 where the index k denotes the phase smoothing iteration step, and $x^{(0)}$
196 is then the reconstructed navigator image from Step I. \mathcal{H} is the Hanning R248.Minor.12
197 window.

198 **III. Shot-combined reconstruction.** Joint reconstruction of all DW im-
199 ages using the shot-combined forward model \mathbf{E}_2 with shot-to-shot phase
200 variation from Step II reads:

$$\operatorname{argmin}_{\tilde{\mathbf{x}}} \|\mathbf{y} - \mathbf{E}_2 \tilde{\mathbf{x}}\|_2^2 + \lambda \|\mathbf{T}(\tilde{\mathbf{x}})\|_* \quad (7)$$

201 Here, LLR regularization was employed in the local spatial-diffusion ma-
202 trices, based on the theory of partially separable functions (Liang, 2007;
203 Trzasko and Manduca, 2011; Zhang et al., 2015). \mathbf{T} represents a linear

operator that firstly slides a local patch window through all DW images
and then flattens every set of local patches to construct two-dimensional
(2D) spatial-diffusion matrices. The spatial dimension equals the block
size, and the diffusion dimension is the number of diffusion encodings.
 $\|\mathbf{T}(\tilde{\mathbf{x}})\|_*$ is the nuclear norm, i.e. the sum of singular values of a spatial-
diffusion matrix. This nuclear norm regularization was accomplished
via singular value thresholding (SVT) of each spatial-diffusion matrix R248.Minor.6
(Cai et al., 2010). After SVT, the adjoint of \mathbf{T} , \mathbf{T}^H , was needed to
reorder pixel values from the spatial-diffusion matrices back to DW im-
ages. To alleviate checkerboard artifacts induced by LLR regularization
with non-overlapping blocks (Hu et al., 2020), we employed overlapping
blocks. In this case, values from overlapping positions are summed up
to the output of \mathbf{T}^H . To enable the correct use of \mathbf{T}^H , we element-wise
divided the output of \mathbf{T}^H by a scaling matrix. This matrix was obtained
via $\mathbf{T}^H(\mathbf{T}(\mathbf{1}))$, where $\mathbf{1}$ denotes the matrix of all ones with the same
shape as the input \mathbf{x} . R249.Minor.9

220 2.6. Reconstruction

221 The acquired raw data was read in by twixtools (<https://github.com/pehses/twixtools>). Ramp-sampling regridding and FOV/2-ghost correc-
222 tion were also performed in twixtools. Subsequently, coil sensitivity maps
223 were computed from reference scans using ESPIRiT (Uecker et al., 2014) in
224 SigPy (Ong and Lustig, 2019).

225 With this pre-processing as well as the implemented forward models and
226 proximal operator, the inverse problem in Eq. (7) was solved by the alter-
227 nating direction method of multipliers (ADMM) (Boyd et al., 2010).

229 ADMM solves the minimization problems in an alternating update scheme,

$$\begin{cases} \mathbf{x}^{(k+1)} := \underset{\mathbf{x}}{\operatorname{argmin}} \| \mathbf{y} - \mathbf{E}(\mathbf{x}) \|^2 + \rho/2 \| \mathbf{T}\mathbf{x} - \mathbf{z}^{(k)} + \mathbf{u}^{(k)} \|_2^2 \\ \mathbf{z}^{(k+1)} := \mathcal{T}_{\lambda/\rho}(\mathbf{T}\mathbf{x}^{(k+1)} + \mathbf{u}^{(k)}) \\ \mathbf{u}^{(k+1)} := \mathbf{u}^{(k)} + \mathbf{T}\mathbf{x}^{(k+1)} - \mathbf{z}^{(k+1)} \end{cases} \quad (8)$$

230 where k denotes the ADMM iteration. \mathbf{z} is the auxiliary variable ($\mathbf{z} = \mathbf{T}\mathbf{x}$),
231 and \mathbf{u} is the Lagrangian multipliers. Importantly, when solving Eq. (2), \mathbf{x}
232 denotes shot images and \mathbf{E} denotes \mathbf{E}_1 in Eq. (8). In contrast, \mathbf{x} denotes shot-
233 combined images and \mathbf{E} denotes \mathbf{E}_2 when solving Eq. (4). \mathbf{x} can be solved
234 using linear least square algorithms, e.g. conjugate gradients (Hestenes and
235 Stiefel, 1952), while \mathbf{z} is updated via singular value thresholding (\mathcal{T}) with
236 the thresholding parameter λ/ρ . The coupling parameter ρ is effective in
237 both the update of \mathbf{x} and \mathbf{z} . It acts as Tikhonov regularization strength
238 when updating \mathbf{x} , but also inversely scales the thresholding strength when
239 updating \mathbf{z} .

240 In this work, 15 ADMM iterations with $\rho = 0.05$ and $\lambda = 0.08$ were used.

241 All reconstructions were done on a single A100 SXM4/NVLink GPU with
242 40 GB memory (NVIDIA, Santa Clara, CA, USA).

243 We compared our proposed joint reconstruction with established multi-
244 shot reconstruction techniques, specifically, MUSE (Chen et al., 2013) and
245 JULEP (Dai et al., 2023), hosted on GitHub by Dr. Dai (Dai et al., 2023).
246 Further, we performed the local-PCA denoising (Cordero-Grande et al., 2019)
247 as implemented in MRtrix (Tournier et al., 2019) on the MUSE reconstructed
248 complex DW images.

249 The in vivo data acquired from Protocol #2 in Table 1 consisted of 126
250 diffusion directions, which exceeds the available GPU memory. Therefore,

251 the 126 data volumes were uniformly split into three parts for our JETS
252 reconstruction with a LLR block width of 6 and the LLR regularization in
253 both Steps I and III in Section 2.5. In addition, MUSE reconstruction was
254 also performed, followed by the local-PCA denoising. Reconstructed DWIs
255 were then processed by DiPy ([Garyfallidis et al., 2014](#)) to obtain color-coded
256 fractional anisotropy (cFA) maps.

257 **3. Results**

258 *3.1. Iterative smoothing of shot-to-shot phase variation*

259 Navigators were acquired with the acceleration rate as listed in Table 1.
260 Besides, the base resolution of navigators (e.g. 32 in Protocol #3 in Table 1)
261 was smaller than imaging echoes. As a result, reconstructed navigator phases
262 (refer to the first column in Fig. 3) from Step I in Section 2.5 are not spatially
263 smooth. Such phases, when used in the shot-combined reconstruction, result
264 in signal void artifacts in DW images. To address this problem, we utilized
265 the iterative smoothing procedure. As shown in Fig. 3, the ripple-like phase
266 artifact disappears after five iterations. It can also be seen that such an R249.Minor.11
267 iterative procedure retains the shot-to-shot phase variation.

– 12

268 *3.2. Comparison to MUSE and JULEP with four-shot iEPI acquisition*

269 The iterative phase smoothing was also applicable to MUSE-type self-
270 navigating reconstruction, where shot phases were reconstructed from imag-
271 ing echoes. Fig. 4 compares our proposed JETS with MUSE (Chen et al.,
272 2013), MUSE with complex-valued local-PCA denoiser (Cordero-Grande et al.,
273 2019), and JULEP (Dai et al., 2023). The residual noise from MUSE can be
274 largely removed by the denoiser. However, when compared to JETS, the de-
275 noiser shows residual noise patterns within the globus pallidus (indicated by
276 the red arrow). JETS also shows better denoising than JULEP. The reason
277 is that JETS enforces spatial-diffusion regularization, whereas JULEP for-
278 mulates structured low-rank regularization of the four shots for one diffusion
279 encoding.

Iterative smoothing of shot-to-shot phase variation

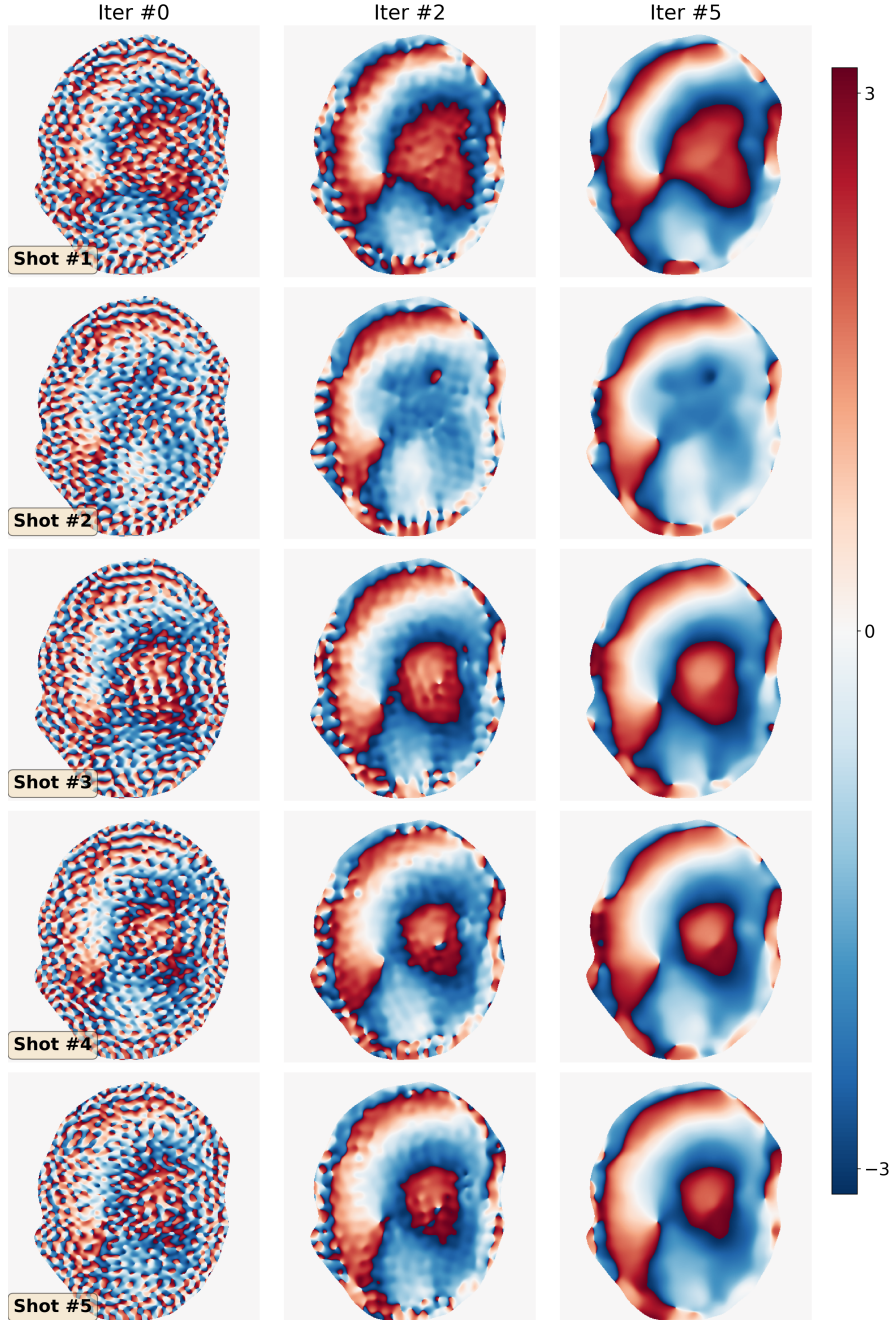


Figure 3: Iterative smoothing of shot-to-shot phase variation according to Eq. (6). Navigators from Protocol #3 were reconstructed based on Step I in Section 2.5 and then used as the input (iter #0, left column).

8th DW image from 4-shot iEPI @ 1 mm ISO

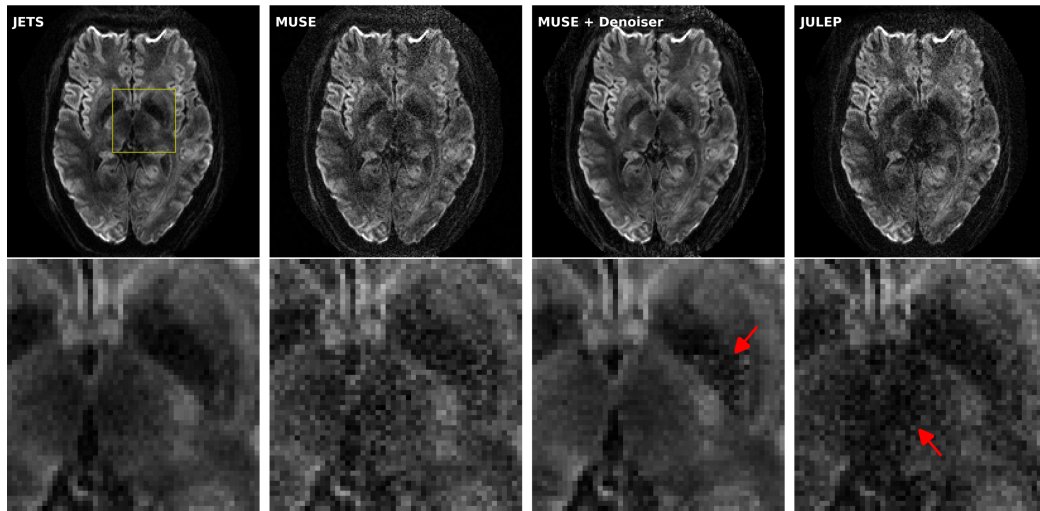


Figure 4: Reconstructed DW images (the 8th diffusion encoding) based on 4-shot iEPI acquisition with 1 mm isotropic resolution (Protocol #1 in Table 1). Four reconstruction methods are compared (from left to right): JETS, MUSE, MUSE with denoiser, and JULEP. The 2nd row displays the magnified views of the yellow square. The image from the denoiser (3rd column) shows residual noise patterns within the globus pallidus (indicated by the red arrow). The JULEP reconstruction (4th column) shows signal dropout in the central region (indicated by the red arrow).

R249.Minor.13

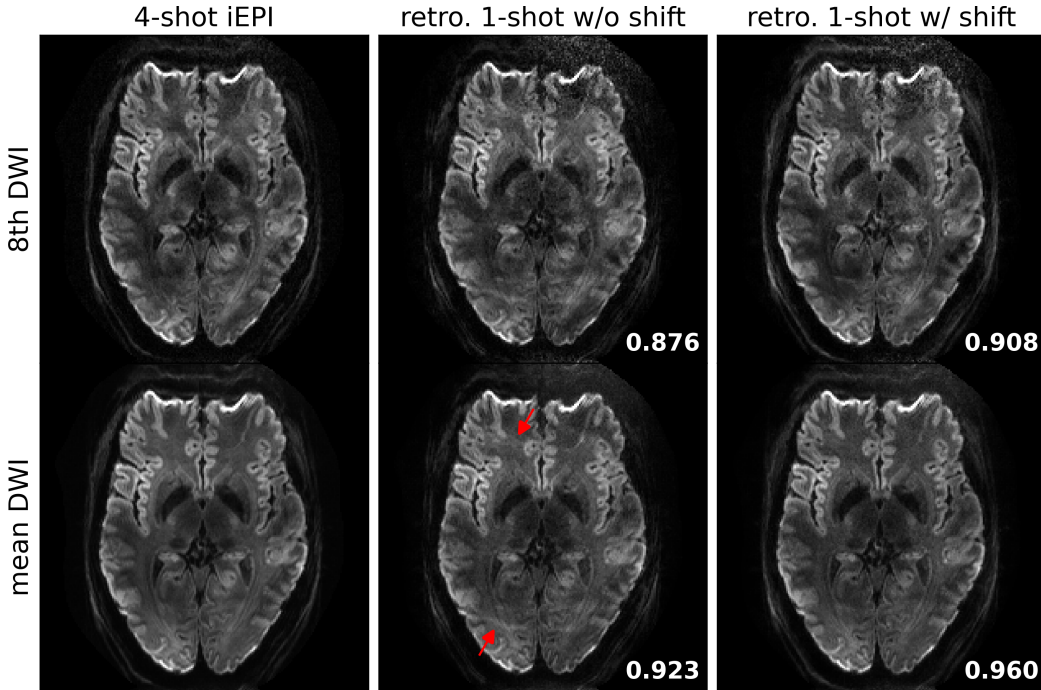


Figure 5: Quantitative validation of the proposed k_y -shift encoding sampling pattern based on 4-shot iEPI acquisition with 1 mm isotropic resolution (Protocol #1 in Table 1). (Top) the 8th diffusion encoding and (bottom) mean DWI over 20 diffusion encodings. (1st column) JETS reconstruction of 4-shot iEPI acquisition is used as the ground truth. The 2nd and the 3rd column displays JETS reconstruction of retrospectively undersampled 1-shot acquisition without and with k_y shifting, respectively. Residual aliasing artifacts are visible in the reconstruction without k_y shifting, as indicated by the red arrows. Structural similarity (SSIM) values are computed and displayed in the bottom right corners.

R249.Minor.14

- 16

280 3.3. Retrospectively undersampling from the four-shot iEPI acquisition

281 JETS reconstruction results on the four-shot prospectively fully-sampled
282 data from Protocol #1 in Table 1, as well as on the retrospectively under-
283 sampled one-shot data without and with the proposed k_y shift are displayed
284 in Fig. 5. Residual aliasing artifacts are visible in the reconstruction without
285 k_y shifting, as indicated by the red arrows. In contrast, the k_y shifting scheme
286 supplies a complementary k - q -space sampling pattern, which is beneficial for
287 joint reconstructions such as JETS. As shown in Fig. 5, JETS results in im-
288 proved SSIM values and reduced aliasing artifacts, when compared to the
289 reconstruction without k_y shifting.

R249.Minor.17,
18, 20

290 3.4. Analysis of reconstruction parameters

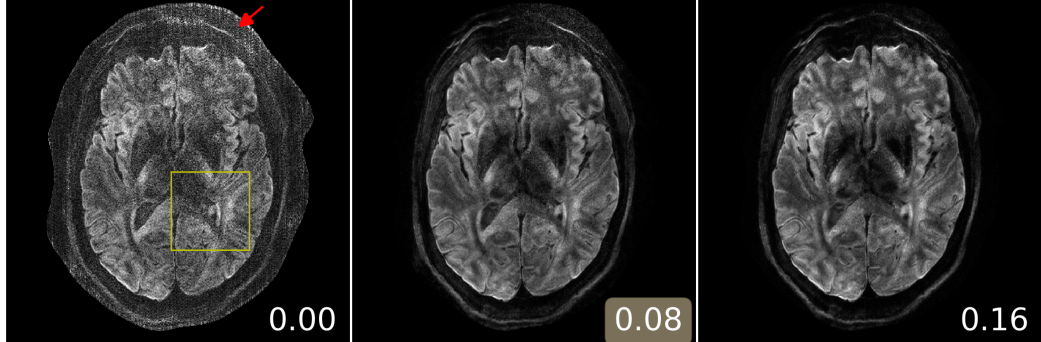
291 Here we provide a systematic analysis of the proposed JETS reconstruc-
292 tion with LLR regularization applied to the spatial-diffusion dimension, as
293 shown in Fig. 6.

294 First, we varied the regularization strength λ . We tested values of 0, 0.08,
295 and 0.16. The reconstruction with $\lambda = 0$ in Eq. (7) corresponds to parallel
296 imaging reconstruction without LLR regularization. It is worth noting that
297 the proposed NAViEPI sequence demonstrates high-quality sub-millimeter
298 DW images ($0.5 \times 0.5 \times 2.0$ mm 3 in this example). The DW images can be
299 further improved with the use of LLR regularization, i.e., reduced noise, as
300 seen in the reconstruction with $\lambda = 0.08$. Increasing λ (e.g. 0.16) further
301 reduces noise, but at the cost of increased blurring. Therefore, $\lambda = 0.08$ was
302 selected in this work.

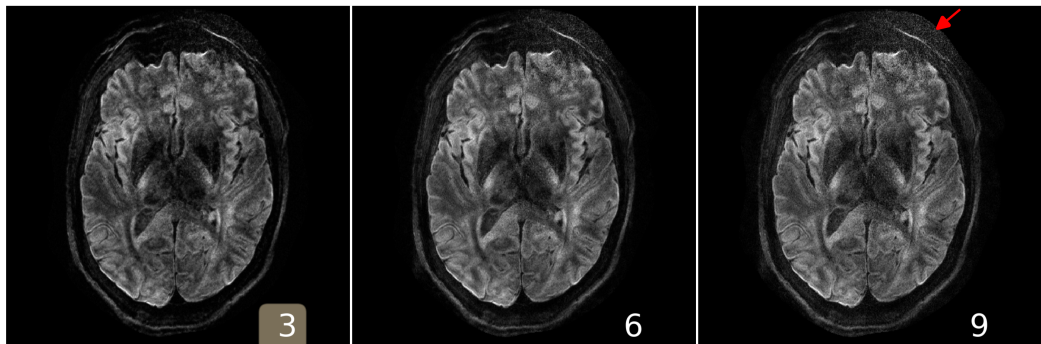
R249.Minor.19

303 Second, besides the regularization strength, the block size (i.e., the area
304 of 2D patches) also plays a role in denoising. We employed square blocks in

(A) varying λ , keeping block as 6 and stride as 1



(B) varying block size, keeping λ as 0.08 and stride as 1



(C) varying stride, keeping λ as 0.08 and block as 6

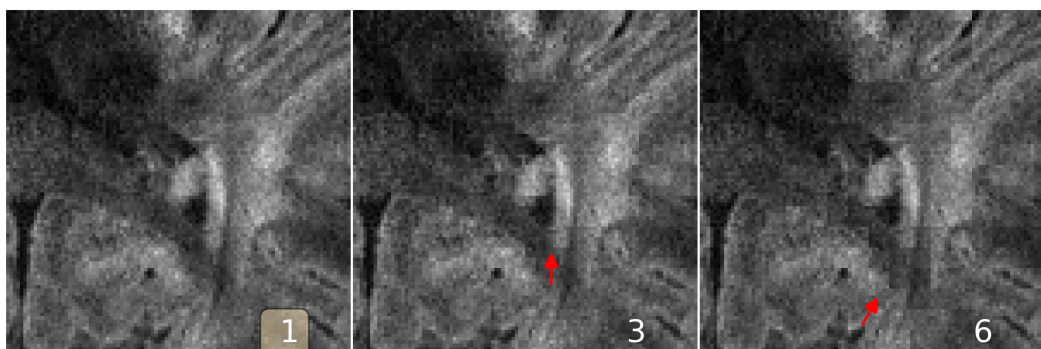


Figure 6: Analysis of reconstruction parameters based on the 3-scan trace acquisition with $0.5 \times 0.5 \times 2.0 \text{ mm}^3$ (Protocol #3 in Table 1). Displayed are JETS reconstructed single-direction DW images. **(A)** Varying the regularization strength λ from 0 to 0.08 and 0.16. **(B)** Varying the block size from 3 to 6 and 9. **(C)** Varying the stride size from 1 to 3 and 6 (non-overlapping).

305 this work. Here, the block width of 2 shows the best denoising as compared
306 to 1 and 3, especially in the peripheral brain region. Among the three tested
307 block widths, the block size of 4 (with the block width 2) is the smallest one
308 which is no smaller than the diffusion directions in this 3-scan trace example
309 ($1 b_0$ plus 3 orthogonal diffusion directions). This observation agrees with
310 the suggestion that the patch size should be no smaller than and close to the
311 diffusion directions (Cordero-Grande et al., 2019).

312 Third, we varied the stride, i.e., the step from one local patch to the
313 next. The use of overlapping LLR (Fig. 6 (C) left) better suppresses blocky
314 artifacts, compared to the partially overlapping LLR (Fig. 6 (C) middle) and
315 the non-overlapping LLR (Fig. 6 (C) right).

R248.Major.4b

316 3.5. Sampling efficiency of NAViEPI

317 As shown in Fig. 7, NAViEPI achieves sub-millimeter resolution (voxel
318 size $0.5 \times 0.5 \times 2.0 \text{ mm}^3$) with the use of a 5-shot acquisition. When compared
319 to a single-shot acquisition with the same voxel size, the acquisition time of
320 NAViEPI is about two times longer, but the image quality of NAViEPI is
321 remarkably improved.

R249.Minor.2¶

322 In the sub-millimeter imaging scenario, the increased base resolution re-
323 quires longer TE (143 ms) in the single-shot acquisition, which results in
324 significant signal loss due to T_2 relaxation. Therefore, sub-millimeter DWI
325 necessitates multi-shot acquisition, which is subject to shot-to-shot phase
326 variation and long scan time. However, NAViEPI solves both challenges. The
327 5-shot acquisition reduces TE to 58 ms, and thus retains SNR significantly
328 compared to the single-shot acquisition. Moreover, the JETS reconstruction
329 can help to reduce noise and improve structural visibility.

3-scan trace acquisition with voxel size $0.5 \times 0.5 \times 2.0 \text{ mm}^3$

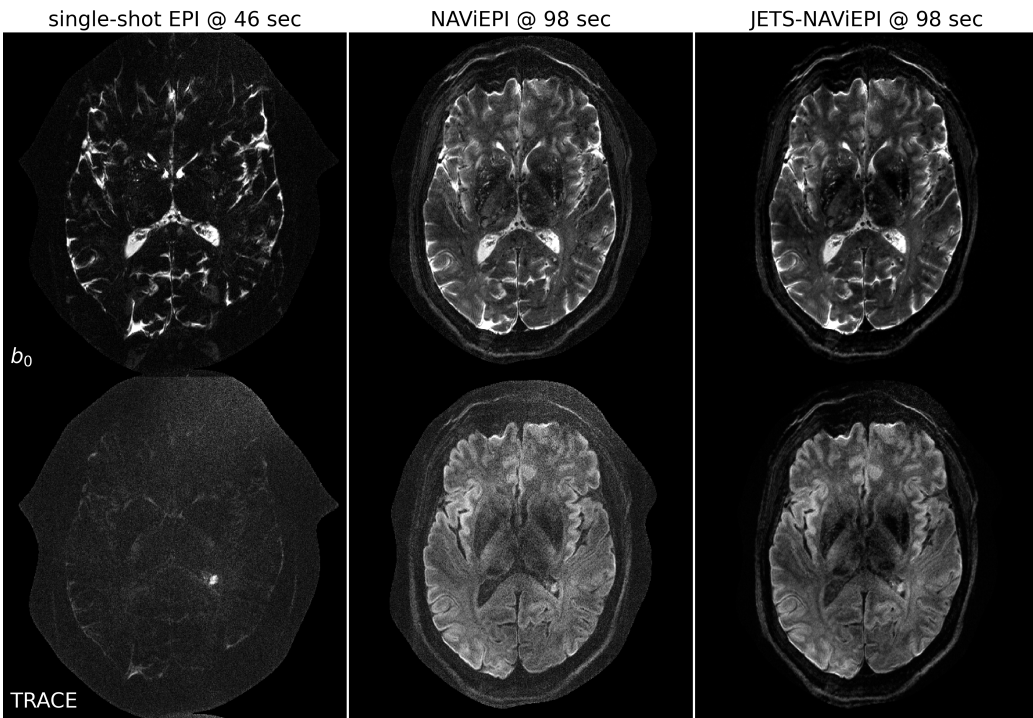


Figure 7: Sampling efficiency of the proposed NAViEPI sequence. 5-shot NAViEPI acquisition with the voxel size $0.5 \times 0.5 \times 2.0 \text{ mm}^3$ (Protocol #3) was compared with single-shot EPI acquisition (Protocol #4). Both the 1st and the 2nd columns were reconstructed via parallel imaging without LLR regularization, whereas the 3rd column was reconstructed via JETS.

3-scan trace acquisition with voxel size $0.5 \times 0.5 \times 2.0 \text{ mm}^3$

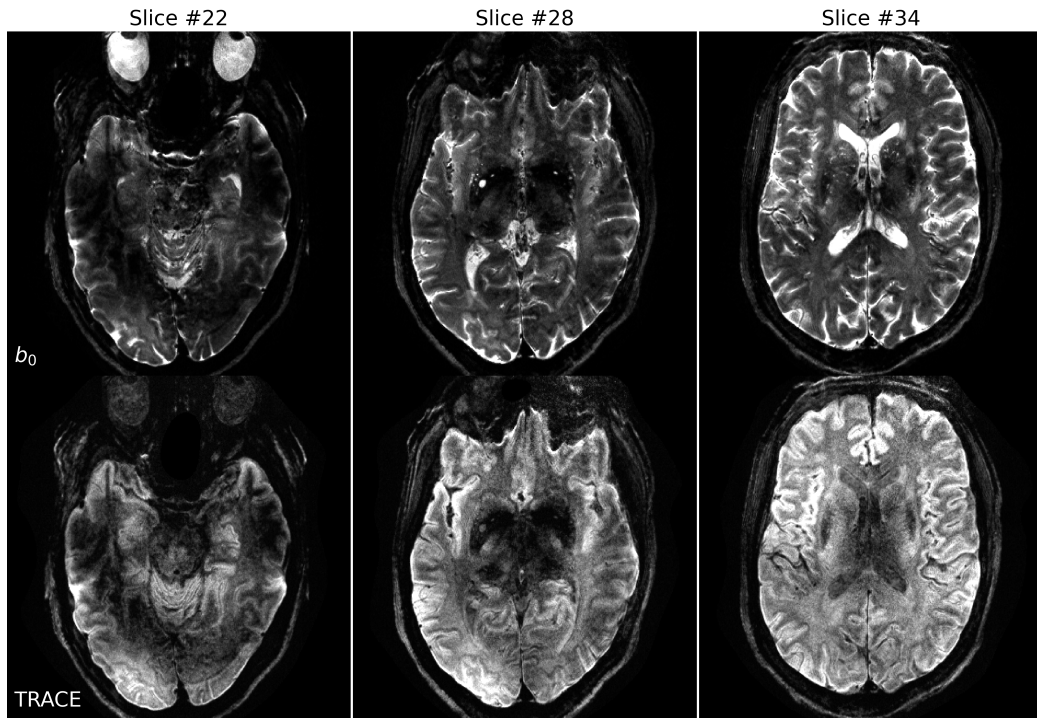


Figure 8: Reconstruction of the 3-scan trace acquisition with the voxel size $0.5 \times 0.5 \times 2.0 \text{ mm}^3$ (Protocol #3) at different slices.

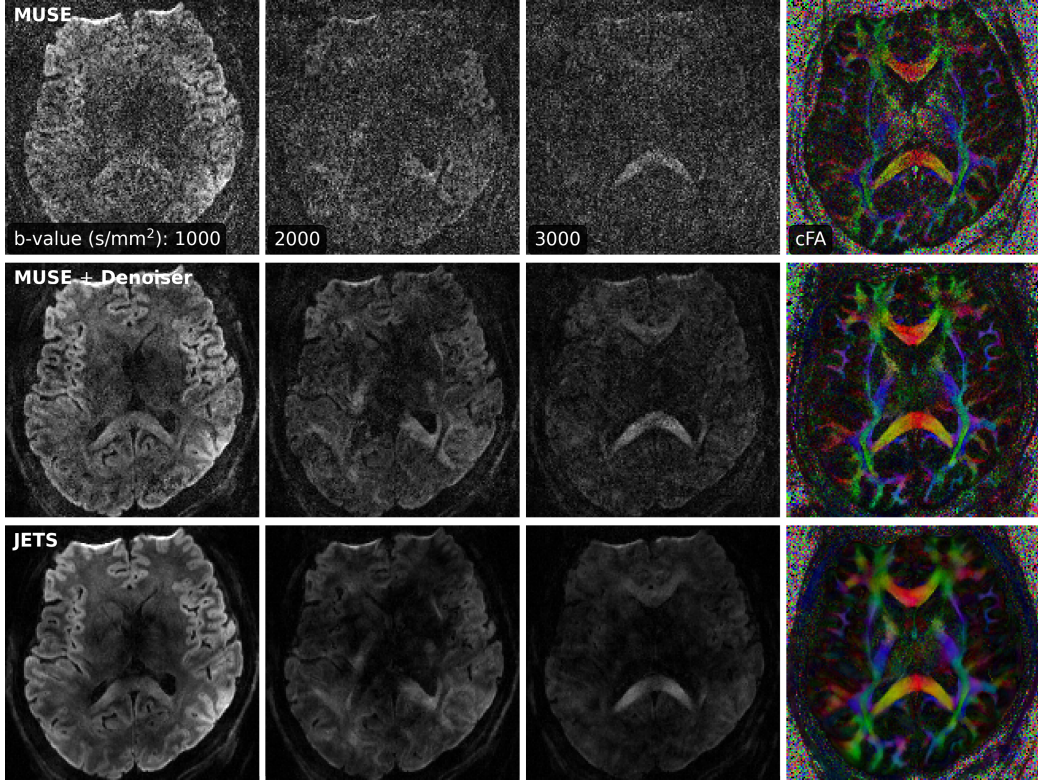


Figure 9: Comparison of three-shell DWIs and cFA maps with data acquired by Protocol #2 in Table 1. Reconstruction methods from top to bottom were MUSE, MUSE with the local-PCA denoiser, and the proposed JETS method.

Fig. 8 shows the JETS reconstructed b_0 and TRACE images in different slice locations. Admittedly, the lower brain region (e.g. slice #22) exhibits inhomogeneous and lower signal intensity than the upper slices. Such inhomogeneity can be alleviated with the use of multi-channel parallel transmission (Katscher et al., 2003; Grissom et al., 2010).

335 *3.6. Diffusion tensor imaging*

336 Protocol #2 in Table 1 yields an acceleration factor of 6×3 per shot, re-
337 sulting in severe noise amplification in MUSE reconstructed DWIs, as shown
338 in Fig. 9. The local-PCA denoiser substantially removes noise, but the DWI
339 at high b -values still illustrates more noise, compared to the proposed JETS
340 reconstruction.

341 4. Discussion

342 This work reports a novel DW-MRI technique, JETS-NAViEPI. NAViEPI
343 (1) achieves the fast and efficient acquisition of both imaging and navigator
344 echoes, (2) enforces consistent effective ESP between the two echoes, and (3)
345 allows for undersampled iEPI as well as a large number of shots. Moreover,
346 compared to the single-shot acquisition, joint k - q -slice reconstruction with k_y -
347 shift encoding on NAViEPI retains SNR and reduces aliasing artifacts in DW
348 images. As a result, JETS-NAViEPI renders high spatiotemporal resolution
349 diffusion MRI protocols in 7 T, e.g., a 3-scan trace acquisition with the voxel
350 size $0.5 \times 0.5 \times 2.0 \text{ mm}^3$ at 1.5 min.

R249.Minor.24

351 One limitation of JETS-NAViEPI is the long reconstruction time due to
352 the simultaneous reconstruction of all DW images and the use of overlapping
353 locally low-rank regularization. The reconstruction for the Protocol #3 in
354 Table 1 on an A100 GPU takes about 2 min per multi-band slice. To reduce
355 the computation time, coil compression algorithms (Buehrer et al., 2007;
356 Huang et al., 2008) can be employed to reduce the number of coils for image
357 reconstruction. Moreover, one can deploy multi-GPU distributed computing
358 or modern optimization algorithms (e.g. stochastic gradient descent) (Ong
359 et al., 2020) to speed up the reconstruction.

360 Neither the signal modeling in Eqs. (2) and (4) nor the LLR regularization
361 considers the subject motion. In the presence of motion, the regularized
362 reconstruction can degrade. To overcome this problem, scout-informed motion
363 estimation and reconstruction (Polak et al., 2022) could be integrated
364 into the framework.

365 Another potential extension of this work is to incorporate distortion cor-

366 rection. The standard distortion correction method is known as TOPUP
367 (Andersson et al., 2003), which acquires two scans with opposing phase-
368 encoding directions to obtain the field inhomogeneity map and then performs
369 conjugate phase reconstruction to correct for distortion. Alternatively, the
370 multi-echo acquisition could be used for the coil sensitivity reference scan,
371 such that both coil sensitivity and B_0 field inhomogeneity maps could be
372 reconstructed from the data.

R249.Minor.25

373 This work employed a single regularization weight λ to enforce low rank-
374 ness along the spatial-diffusion direction. However, SNR may be heteroge-
375 neous within the FOV. Therefore, one single regularization scalar may be
376 inadequate to cover the whole FOV. Beyond this SVT-based reconstruction,
377 one can seek to use machine learning to learn a q -space prior as the regularizer
378 (Hammernik et al., 2018; Lam et al., 2019; Mani et al., 2021).

R249.Minor.26

379 Although NAViEPI employs navigators for the acquisition of shot-to-
380 shot phase variation, it is worth noting that phase behavior depends on
381 several hard-to-control factors such as pulsatile motion, bulk motion, loca-
382 tions within the brain, and diffusion sensitization strength. Therefore, more
383 comprehensive modeling or post-processing such as image registration can
384 be considered in future work.

385 This work compared LLR regularized JETS to MUSE post-processed by
386 the local PCA denoiser (Cordero-Grande et al., 2019). Technically, the LLR
387 regularization is realized by soft thresholding of the singular values of the
388 spatial-diffusion matrices, whereas the denoiser performs hard thresholding.
389 Both approaches demonstrate effective noise removal. In the scenario of ac-
390 celerated acquisitions, one can employ both approaches to maximally boost

R248.3b

391 SNR, i.e., the use of LLR regularization for image reconstruction followed by
392 the denoiser as a post-processing step.

393 While this work reconstructs all DW images and then performs model
394 fitting, an alternative approach is to directly estimate b_0 and diffusion ten-
395 sors from measured k - q -space data using model-based reconstruction (Knoll
396 et al., 2015; Dong et al., 2018; Shafieizargar et al., 2023). Compared to DW
397 image reconstruction, model-based reconstruction solves for a fewer number
398 of unknowns, but requires strict diffusion tensor modeling and the use of
399 nonlinear least square solvers.

400 **5. Conclusions**

401 We demonstrated the JETS-NAViEPI technique, which integrates a k_y -
402 shifted encoding interleaved EPI sequence and a joint reconstruction with
403 overlapping locally low-rank regularization for high spatial-angular-temporal
404 resolution DW-MRI at 7 T. This technique allows for high-quality DW image
405 reconstruction with accelerated acquisitions.

406 **Funding**

407 Funding by the German Research Foundation (DFG) is gratefully ac-
408 knowledged (projects 513220538, 512819079; and project 500888779 of the
409 RU5534 MR biosignatures at UHF). In addition, funding by the National
410 Institutes of Health (NIH), R01 EB024532 and P41 EB017183, is gratefully
411 acknowledged.

412 **Data and code available statement**

413 In the spirit of reproducible and open science, we publish our source
414 code (<https://github.com/ZhengguoTan/sigpy>) as well as the raw k -space
415 data (<https://doi.org/10.5281/zenodo.7548595>). We also provide inter- R248.8
416 active demonstrations of the reconstruction procedure (https://github.com/ZhengguoTan/demo_jets_diffusion_mri_7t).
417

418 **Acknowledgments**

419 The authors gratefully acknowledge the scientific support and HPC re-
420 sources provided by the Erlangen National High Performance Computing
421 Center (NHR@FAU) of Friedrich-Alexander-Universität Erlangen-Nürnberg
422 (FAU) under the NHR project b143dc. NHR funding is provided by federal
423 and Bavarian state authorities. NHR@FAU hardware is partially funded by
424 the German Research Foundation (DFG) – 440719683.

425 The authors thank Dr. Peter Neher for the discussion on MITK-Diffusion.
426 The authors thank Dr. Berkin Bilgic for making the MUSSELS source code
427 (<https://bit.ly/2QgBg9U>) publically available, Dr. Erpeng Dai for sharing
428 the JULEP source code (<https://github.com/daiep/JULEP>) on GitHub,
429 and Dr. Zhiyong Zhang for sharing the SPA-LLR source code (<https://github.com/ZZgroupSJTU/PMCmsDTI>) on GitHub. The authors also thank
430 Dr. Philipp Ehses for the discussion on twixtools (<https://github.com/pehses/twixtools>).
431
432

433 **References**

- 434 Andersson, J.L.R., Skare, S., Ashburner, J., 2003. How to correct suscepti-
435 bility distortions in spin-echo echo-planar images: application to diffusion
436 tensor imaging. NeuroImage 20, 870–888. doi:[10.1016/S1053-8119\(03\)00336-7](https://doi.org/10.1016/S1053-8119(03)00336-7).
- 438 Bammer, R., Keeling, S.L., Augustin, M., Pruessmann, K.P., Wolf, R., Stoll-
439 berger, R., Hartung, H.P., Fazekas, F., 2001. Improved diffusion-weighted
440 single-shot echo-planar imaging (EPI) in stroke using sensitivity encoding
441 (SENSE). Magn. Reson. Med. 46, 548–554. doi:[10.1002/mrm.1226](https://doi.org/10.1002/mrm.1226).
- 442 Basser, P.J., Mattiello, J., Le Bihan, D., 1994. MR diffusion tensor
443 spectroscopy and imaging. Biophys. J. 66, 259–267. doi:[10.1016/S0006-3495\(94\)80775-1](https://doi.org/10.1016/S0006-3495(94)80775-1).
- 445 Bilgic, B., Chatnuntawech, I., Manhard, M.K., Tian, Q., Liao, C., Iyer, S.S.,
446 Cauley, S.F., Huang, S.Y., Polimeni, J.R., Wald, L.L., Setsompop, K.,
447 2019. Highly accelerated multishot echo planar imaging through synergistic
448 machine learning and joint reconstruction. Magn. Reson. Med. 82, 1343–
449 1358. doi:[10.1002/mrm.27813](https://doi.org/10.1002/mrm.27813).
- 450 Block, K.T., Uecker, M., Frahm, J., 2007. Undersampled radial MRI with
451 multiple coils. Iterative image reconstruction using a total variation con-
452 straint. Magn. Reson. Med. 57, 1186–1098. doi:[10.1002/mrm.21236](https://doi.org/10.1002/mrm.21236).
- 453 Boyd, S., Parikh, N., Chu, E., Peleato, B., Eckstein, J., 2010. Distributed
454 optimization and statistical learning via the alternating direction method

- 455 of multipliers. Foundations and Trends in Machine Learning 3, 1–122.
456 doi:[10.1561/2200000016](https://doi.org/10.1561/2200000016).
- 457 Breuer, F.A., Blaimer, M., Heidemann, R.M., Mueller, M.F., Griswold, M.A.,
458 Jakob, P.M., 2005. Controlled aliasing in parallel imaging results in higher
459 acceleration (CAPIRINHA) for multi-slice imaging. Magn. Reson. Med.
460 53, 684–691. doi:[10.1002/mrm.20401](https://doi.org/10.1002/mrm.20401).
- 461 Buehrer, M., Pruessmann, K.P., Boesiger, P., Kozerke, S., 2007. Array com-
462 pression for MRI with large coil arrays. Magn. Reson. Med 57, 1131–1139.
463 doi:[10.1002/mrm.21237](https://doi.org/10.1002/mrm.21237).
- 464 Butts, K., Riederer, S.J., Ehman, R.L., Thompson, R.M., Jack, C.R., 1993.
465 Interleaved echo planar imaging on a standard MRI system. Magn. Reson.
466 Med. 31, 67–72. doi:[10.1002/mrm.1910310111](https://doi.org/10.1002/mrm.1910310111).
- 467 Cai, J.F., Candès, E.J., Shen, Z., 2010. A singular value threshold-
468 ing algorithm for matrix completion. SIAM. J. Optim. 20, 1956–1982.
469 doi:[10.1137/080738970](https://doi.org/10.1137/080738970).
- 470 Chen, N.K., Guidon, A., Chang, H.C., Song, A.W., 2013. A robust multi-
471 shot scan strategy for high-resolution diffusion weighted MRI enabled by
472 multiplexed sensitivity-encoding (MUSE). NeuroImage 72, 41–47. doi:[10.1016/j.neuroimage.2013.01.038](https://doi.org/10.1016/j.neuroimage.2013.01.038).
- 474 Cordero-Grande, L., Christiaens, D., Hutter, J., Price, A.N., Hajnal, J.V.,
475 2019. Complex diffusion-weighted image estimation via matrix recovery
476 under general noise models. NeuroImage 200, 391–404. doi:[10.1016/j.neuroimage.2019.06.039](https://doi.org/10.1016/j.neuroimage.2019.06.039).

- 478 Dai, E., Ma, X., Zhang, Z., Yuan, C., Guo, H., 2017. Simultaneous multislice
479 accelerated interleaved EPI DWI using generalized blipped-CAIPI acqui-
480 sition and 3D K-space reconstruction. Magn. Reson. Med. 77, 1593–1605.
481 doi:[10.1002/mrm.26249](https://doi.org/10.1002/mrm.26249).
- 482 Dai, E., Mani, M., McNab, J.A., 2023. Multi-band multi-shot diffu-
483 sion MRI reconstruction with joint usage of structured low-rank con-
484 straints and explicit phase mapping. Magn. Reson. Med. 89, 95–111.
485 doi:[10.1002/mrm.29422](https://doi.org/10.1002/mrm.29422).
- 486 Dai, E., Zhang, Z., Ma, X., Dong, Z., Li, X., Xiong, Y., Yuan, C., Guo, H.,
487 2018. The effects of navigator distortion and noise level on interleaved EPI
488 DWI reconstruction: a comparison between image- and *k*-space method.
489 Magn. Reson. Med. 80, 2024–2032. doi:[10.1002/mrm.27190](https://doi.org/10.1002/mrm.27190).
- 490 Dong, Z., Dai, E., Wang, F., Zhang, Z., Ma, X., Yuan, C., Guo, H., 2018.
491 Model-based reconstruction for simultaneous multislice and parallel imag-
492 ing accelerated multishot diffusion tensor imaging. Med. Phys. 45, 3196–
493 3204. doi:[10.1002/mp.12974](https://doi.org/10.1002/mp.12974).
- 494 Garyfallidis, E., Brett, M., Amirbekian, B., Rokem, A., van der Walt, S.,
495 Descoteaux, M., Nimmo-Smith, I., Contributors, D., 2014. DIPY, a library
496 for the analysis of diffusion MRI data. Front. Neuroinform. 8, 1–17. doi:[10.3389/fninf.2014.00008](https://doi.org/10.3389/fninf.2014.00008).
- 498 Grissom, W.A., Sacolick, L., Vogel, M.W., 2010. Improving high-field MRI
499 using parallel excitation. Imaging Med. 2, 675–693. doi:[10.2217/IIM.10.62](https://doi.org/10.2217/IIM.10.62).

- 501 Griswold, M.A., Jakob, P.M., Heidemann, R.M., Nittka, M., Jellus, V.,
502 Wang, J., Kiefer, B., Haase, A., 2002. Generalized autocalibrating par-
503 tially parallel acquisitions (GRAPPA). Magn. Reson. Med. 47, 1202–1210.
504 doi:[10.1002/mrm.10171](https://doi.org/10.1002/mrm.10171).
- 505 Guhaniyogi, S., Chu, M.L., Chang, H.C., Song, A.W., Chen, N.K., 2016. Mo-
506 tion immune diffusion imaging using augmented MUSE for high-resolution
507 multi-shot EPI. Magn. Reson. Med. 75, 639–652. doi:[10.1002/mrm.25624](https://doi.org/10.1002/mrm.25624).
- 508 Hammernik, K., Klatzer, T., Kobler, E., Recht, M.P., Sodickson, D.K., Pock,
509 T., Knoll, F., 2018. Learning a variational network for reconstruction of
510 accelerated MRI data. Magn. Reson. Med. 79, 3055–3071. doi:[10.1002/mrm.26977](https://doi.org/10.1002/mrm.26977).
- 512 Heidemann, R.M., Porter, D.A., Anwander, A., Feiweier, T., Heberlein, K.,
513 Knösche, T.R., Turner, R., 2010. Diffusion imaging in humans at 7 T
514 using readout-segmented EPI and GRAPPA. Magn. Reson. Med. 64, 9–
515 14. doi:[10.1002/mrm.22480](https://doi.org/10.1002/mrm.22480).
- 516 Hestenes, M.R., Stiefel, E., 1952. Methods of conjugate gradients for solving
517 linear systems. J. Res. Natl. Bur. Stand. 49, 409–436. doi:[10.6028/jres.049.044](https://doi.org/10.6028/jres.049.044).
- 519 Hu, Y., Wang, X., Tian, Q., Yang, G., Daniel, B., McNab, J., Hargreaves, B.,
520 2020. Multi-shot diffusion-weighted MRI reconstruction with magnitude-
521 based spatial-angular locally low-rank regularization (SPA-LLR). Magn.
522 Reson. Med. 83, 1596–1607. doi:[10.1002/mrm.28025](https://doi.org/10.1002/mrm.28025).

- 523 Huang, F., Vijayakumar, S., Li, Y., Hertel, S., Duensing, G.R., 2008. A soft-
524 ware channel compression technique for faster reconstruction with many
525 channels. *Magn. Reson. Imaging* 26, 133–141. doi:[10.1016/j.mri.2007.04.010](https://doi.org/10.1016/j.mri.2007.04.010).
- 527 Jeong, H.K., Gore, J.C., Anderson, A.W., 2013. High-resolution human
528 diffusion tensor imaging using 2-D navigated multishot SENSE EPI at 7
529 T. *Magn. Reson. Med.* 69, 793–802. doi:[10.1002/mrm.24320](https://doi.org/10.1002/mrm.24320).
- 530 Jones, D.K., 2010. Diffusion MRI: Theory, methods, and applications. Oxford
531 University Press. doi:[10.1093/med/9780195369779.001.0001](https://doi.org/10.1093/med/9780195369779.001.0001).
- 532 Katscher, U., Börnert, P., Leussler, C., van den Brink, J.S., 2003. Transmit
533 SENSE. *Magn. Reson. Med.* 49, 144–150. doi:[10.1002/mrm.10353](https://doi.org/10.1002/mrm.10353).
- 534 Knoll, F., Raya, J.G., Halloran, R.O., Baete, S., Sigmund, E., Bammer, R.,
535 Block, T., Otazo, R., Sodickson, D.K., 2015. A model-based reconstruction
536 for undersampled radial spin-echo DTI with variational penalties on the
537 diffusion tensor. *NMR Biomed* 28, 353–366. doi:[10.1002/nbm.3258](https://doi.org/10.1002/nbm.3258).
- 538 Lam, F., Li, Y., Peng, X., 2019. Constrained magnetic resonance spectro-
539 scopic imaging by learning nonlinear low-dimensional models. *IEEE Trans.*
540 *Med. Imaging* 39, 545–555. doi:[10.1109/TMI.2019.2930586](https://doi.org/10.1109/TMI.2019.2930586).
- 541 Le Bihan, D., Breton, E., Lallemand, D., Grenier, P., Cabanis, E., Laval-
542 Jeantet, M., 1986. MR imaging of intravoxel incoherent motions: appli-
543 cation to diffusion and perfusion in neurologic disorders. *Radiology* 161,
544 401–407. doi:[10.1148/radiology.161.2.3763909](https://doi.org/10.1148/radiology.161.2.3763909).

- 545 Liang, Z.P., 2007. Spatiotemporal imaging with partially separable functions,
546 in: 2007 4th IEEE International Symposium on Biomedical Imaging: From
547 Nano to Macro, pp. 988–991. doi:[10.1109/ISBI.2007.357020](https://doi.org/10.1109/ISBI.2007.357020).
- 548 Liu, C., Moseley, M.E., Bammer, R., 2005. Simultaneous phase cor-
549 rection and SENSE reconstruction for navigated multi-shot DWI with
550 non-Cartesian k -space sampling. Magn. Reson. Med. 54, 1412–1422.
551 doi:[10.1002/mrm.20706](https://doi.org/10.1002/mrm.20706).
- 552 Lustig, M., Donoho, D., Pauly, J.M., 2007. Sparse MRI: The application of
553 compressed sensing for rapid MR imaging. Magn. Reson. Med. 58, 1182–
554 1195. doi:[10.1002/mrm.21391](https://doi.org/10.1002/mrm.21391).
- 555 Mani, M., Jacob, M., Kelley, D., Magnotta, V., 2017. Multi-shot sensitivity-
556 encoded diffusion data recovery using structured low-rank matrix comple-
557 tion (MUSSELS). Magn. Reson. Med. 78, 494–507. doi:[10.1002/mrm.26382](https://doi.org/10.1002/mrm.26382).
- 559 Mani, M., Magnotta, V.A., Jacob, M., 2021. qModeL: A plug-and-play
560 model-based reconstruction for highly accelerated multi-shot diffusion MRI
561 using learned priors. Magn. Reson. Med. 86, 835–851. doi:[10.1002/mrm.28756](https://doi.org/10.1002/mrm.28756).
- 563 Mansfield, P., 1977. Multi-planar image formation using NMR spin echoes.
564 J Phys C 10, 55–58. doi:[10.1088/0022-3719/10/3/004](https://doi.org/10.1088/0022-3719/10/3/004).
- 565 Maudsley, A.A., 1980. Multiple-line-scanning spin density imaging. J. Magn.
566 Reson. 41, 112–126. doi:[10.1016/0022-2364\(80\)90207-3](https://doi.org/10.1016/0022-2364(80)90207-3).

- 567 Merboldt, K.D., Hanicke, W., Frahm, J., 1985. Self-diffusion NMR imaging using stimulated echoes. *J. Magn. Reson.* 64, 479–486. doi:[10.1016/0022-2364\(85\)90111-8](https://doi.org/10.1016/0022-2364(85)90111-8).
- 570 Mori, S., Crain, B.J., Chacko, V.P., Van Zijl, P.C.M., 1999. Three-dimensional tracking of axonal projections in the brain by magnetic resonance imaging. *Ann. Neurol.* 45, 265–269. doi:[10.1002/1531-8249\(199902\)45:2<265::AID-ANA21>3.0.CO;2-3](https://doi.org/10.1002/1531-8249(199902)45:2<265::AID-ANA21>3.0.CO;2-3).
- 574 Ong, F., Lustig, M., 2019. SigPy: A Python package for high performance iterative reconstruction, in: Proceedings of the 27th Annual Meeting of ISMRM, Montréal, CAN, p. 4819. doi:[10.5281/zenodo.5893788](https://doi.org/10.5281/zenodo.5893788).
- 577 Ong, F., Zhu, X., Cheng, J.Y., Johnson, K.M., Larson, P.E.Z., Vasanawala, S.S., Lustig, M., 2020. Extreme MRI: Large-scale volumetric dynamic imaging from continuous non-gated acquisitions. *Magn. Reson. Med.* 84, 1763–1780. doi:[10.1002/mrm.28235](https://doi.org/10.1002/mrm.28235).
- 581 Pipe, J.G., Farthing, V.G., Forbes, K.P., 2002. Multishot diffusion-weighted FSE using PROPELLER MRI. *Magn. Reson. Med.* 47, 42–52. doi:[10.1002/mrm.10014](https://doi.org/10.1002/mrm.10014).
- 584 Polak, D., Splitthoff, D.N., Clifford, B., Lo, W.C., Huang, S.Y., Conklin, J., Wald, L.L., Setsompop, K., Cauley, S., 2022. Scout accelerated motion estimation and reduction (SAMER). *Magn. Reson. Med.* 87, 163–178. doi:[10.1002/mrm.28971](https://doi.org/10.1002/mrm.28971).
- 588 Porter, D.A., Heidemann, R.M., 2009. High resolution diffusion-weighted imaging using readout-segmented echo-planar imaging, parallel imaging

- 590 and a two-dimensional navigator-based reacquisition. Magn. Reson. Med.
591 62, 468–475. doi:[10.1002/mrm.22024](https://doi.org/10.1002/mrm.22024).
- 592 Pruessmann, K.P., Weiger, M., Scheidegger, M.B., Boesiger, P., 1999.
593 SENSE: Sensitivity encoding for fast MRI. Magn. Reson. Med. 42, 952–
594 962. doi:[10.1002/\(SICI\)1522-2594\(199911\)42:5<952::AID-MRM16>3.0.CO;2-S](https://doi.org/10.1002/(SICI)1522-2594(199911)42:5<952::AID-MRM16>3.0.CO;2-S).
- 595
- 596 Ra, J.B., Rim, C.Y., 1993. Fast imaging using subencoding data sets from
597 multiple detectors. Magn. Reson. Med. 30, 142–145. doi:[10.1002/mrm.1910300123](https://doi.org/10.1002/mrm.1910300123).
- 598
- 599 Roemer, P.B., Edelstein, W.A., Hayes, C.E., Souza, S.P., Mueller, O.M.,
600 1990. The NMR phased array. Magn. Reson. Med. 16, 192–225. doi:[10.1002/mrm.1910160203](https://doi.org/10.1002/mrm.1910160203).
- 601
- 602 Setsompop, K., Fan, Q., Stockmann, J., Bilgic, B., Huang, S., Cauley, S.F.,
603 Nummenmaa, A., Wang, F., Rathi, Y., Witzel, T., Wald, L.L., 2018. High-
604 resolution *in vivo* diffusion imaging of the human brain with generalized
605 slice dithered enhanced resolution: Simultaneous multislice (gSlider-SMS).
606 Magn. Reson. Med. 79, 141–151. doi:[10.1002/mrm.26653](https://doi.org/10.1002/mrm.26653).
- 607
- 608 Setsompop, K., Gagoski, B.A., Polimeni, J.R., Witzel, T., Wedeen, V.J.,
609 Wald, L.L., 2012. Blipped-controlled aliasing in parallel imaging for si-
multaneous multislice echo planar imaging with reduced *g*-factor penalty.
610 Magn. Reson. Med. 67, 1210–1224. doi:[10.1002/mrm.23097](https://doi.org/10.1002/mrm.23097).
- 611
- 612 Shafieizargar, B., Jeurissen, B., Poot, D.H.J., Klein, S., Van Audekerke,
J., Verhoye, M., den Dekker, A.J., Sijbers, J., 2023. ADEPT: Accurate

- 613 diffusion echo-planar imaging with multi-contrast shoTs. Magn. Reson.
614 Med. 89, 396–410. doi:[10.1002/mrm.29398](https://doi.org/10.1002/mrm.29398).
- 615 Tournier, J.D., Smith, R., Raffelt, D., Tabbara, R., Dhollander, T., Pietsch,
616 M., Christiaens, D., Jeurissen, B., Yeh, C.H., Connelly, A., 2019. MRtrix3:
617 A fast, flexible and open software framework for medical image processing
618 and visualisation. NeuroImage 202, 116137. doi:<https://doi.org/10.1016/j.neuroimage.2019.116137>.
- 620 Trzasko, J., Manduca, A., 2011. Local versus global low-rank promotion in
621 dynamic MRI series reconstruction, in: Proceedings of the 19th Annual
622 Meeting of ISMRM, Montréal, CAN, p. 4371.
- 623 Tuch, D.S., Reese, T.G., Wiegell, M.R., Makris, N., Belliveau, J.W., Wedeen,
624 V.J., 2002. High angular resolution diffusion imaging reveals intravoxel
625 white matter fiber heterogeneity. Magn. Reson. Med. 48, 577–582. doi:[10.1002/mrm.10268](https://doi.org/10.1002/mrm.10268).
- 627 Uecker, M., Lai, P., Murphy, M.J., Virtue, P., Elad, M., Pauly, J.M.,
628 Vasanawala, S.S., Lustig, M., 2014. ESPIRiT – an eigenvalue approach
629 to autocalibrating parallel MRI: Where SENSE meets GRAPPA. Magn.
630 Reson. Med. 71, 990–1001. doi:[10.1002/mrm.24751](https://doi.org/10.1002/mrm.24751).
- 631 Wu, W., Koopmans, P.J., Andersson, J.L., Miller, K.L., 2019. Diffusion
632 Acceleration with Gaussian process Estimated Reconstruction (DAGER).
633 Magn. Reson. Med. 82, 107–125. doi:[10.1002/mrm.27699](https://doi.org/10.1002/mrm.27699).
- 634 Wu, W., Miller, K.L., 2017. Image formation in diffusion MRI: A review

635 of recent technical developments. J. Magn. Reson. Imaging 46, 646–662.
636 doi:[10.1002/jmri.25664](https://doi.org/10.1002/jmri.25664).

637 Zhang, T., Pauly, J.M., Levesque, I.R., 2015. Accelerated parameter mapping
638 with a locally low rank constraint. Magn. Reson. Med. 73, 655–661. doi:[10.](https://doi.org/10.1002/mrm.25161)
639 [10.1002/mrm.25161](https://doi.org/10.1002/mrm.25161).